Composites Part C: Open Access 5 (2021) 100146

Contents lists available at ScienceDirect

Composites Part C: Open Access

journal homepage: www.elsevier.com/locate/jcomc

Damage tolerance and notch sensitivity of bio-inspired thin-ply Bouligand structures

Johann Körbelin[a,*], Philip Goralski[a], Benedikt Kötter[a], Florian Bittner[b], Hans-Josef Endres[b], Bodo Fiedler[a]

[a] Hamburg University of Technology, Institute of Polymer and Composites, Denickestraße 15, 21073 Hamburg, Germany
[b] Leibniz University Hannover, Institute of Plastics and Circular Economy IKK, An der Universität 2, 30823 Garbsen, Germany

ARTICLE INFO

Keywords:
Layered structures
Microstructures
Stress concentrations
CT analysis
Failure
Hybrid

ABSTRACT

Different bio-inspired Bouligand thin-ply Carbon-Fibre-Reinforced Plastic (CFRP) laminates with a pitch angle as low as 2.07° are realised, which is the smallest pitch angle realised in literature. The angle is therefore close angles found in biological microstructures. Low-Velocity Impact (LVI) and residual compressive strength tests determined the damage tolerance of the structures. Investigated were two different interlaminar fracture toughnesses and two different metal-Bouligand-CFRP-layups. The low pitch angle results in significantly higher residual strengths than 45° quasi-isotropic (QI) layups, despite the significantly lower proportion of 0° fibres. Higher fracture toughness and hybridisation with steel layers lead to reduced matrix damage without increasing residual compressive strength. In-plane plane tension properties are determined with a pitch angle of 2.59°. The results reveal, that the unnotched tensile strength is significantly lower. However, only helicoidal, sub-critical matrix cracking and no delaminations occur before final failure. The sub-critical matrix cracking leads to almost no notch sensitivity and a similar open-hole-tensile strength to 45°-QI layups despite the low number of 0°-fibres.

1. Introduction

Fibre-reinforced plastics (FRP) exhibit complex failure mechanisms, due to their multi-scale nature and different constituents. Matrix-cracks, delamination and fibre failure can occur and interact with each other, as failure on micro-level influences the failure process at all higher levels. Not only the constituents are defining the laminate strength and failure process, but also laminate design. In particular, the interaction between the layup and layer thickness has a decisive influence on the failure behaviour. A fairly new approach to control the damage behaviour of FRP is the use of advanced layup designs inspired by nature. FRP Structures in safety-critical applications are subjected to high requirements on damage tolerance, as some level of damage must be assumed to exist in the composite structure [1–3]. Impact loading is of particular interest because the layered structure of composites results in low out-of-plane strength. Impacts usually lead to the formation of local damage, reducing strength and stiffness of the laminate. Especially in CFRP Structures damages induced by LVI are hard to detect visually. These damages are so-called, barely visible damage (BVID).

A promising approach are helicoidal laminates structures found in impact-loaded body parts of some animals, which are called Bouligand structure. Bouligand [4] described in the early 1970's twisted fibre structures in highly impact stressed body parts of insects, beetles or spiders. Prominent use of the the Bouligand structures are the dactyl clubs of the mantis shrimp. The clubs are used as a biological hammer, for example to smash the shells or carapaces of maritime organisms. The clubs exhibit an impressive set of characteristics adapted for surviving high energy impacts [5]. Despite the high loads, the dactyl clubs are extremely damage tolerant as they can withstand thousands of impacts [6]. A cross-sectional analysis of the club by Weaver [6] divides it in different distinct structural domains. The load introduction area of the club is divided into an impact region and a periodic region which micro structure is similar to a Bouligand structure. The pitch angle in the periodic region of the dactyl clubs varies and was approximated by Gruenfelder et al. [7] between the layers in the outer region with 1.6° and in the inner region with 6.2°.

Fig. 1 displays a symmetrical Bouligand laminate structure consisting of two Bouligand units. It is a UD-laminate structure which features a very small fibre angle difference or pitch angle and therefore a rotating helicoidal fibre angle in the thickness direction. The realisation of truly nature-like Bouligand structure is only possible since the development of "thin-ply" laminates, which are characterised by a layer thickness of less than 60$^{\mu m}$. These layer thicknesses became available through the ad-

* Corresponding author.
E-mail address: johann.koerbelin@tuhh.de (J. Körbelin).
URL: https://www.tuhh.de/kvweb (J. Körbelin)

https://doi.org/10.1016/j.jcomc.2021.100146
Received 23 February 2021; Received in revised form 25 March 2021; Accepted 17 April 2021

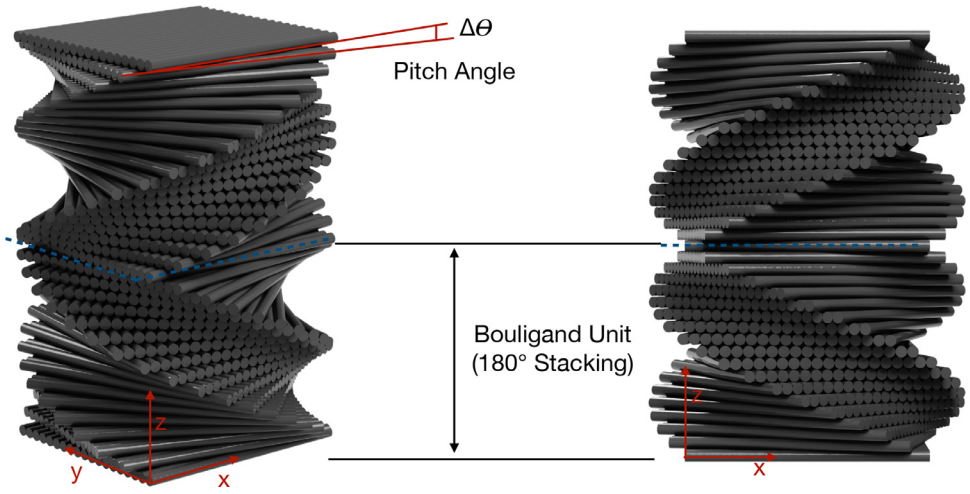

Fig. 1. Schematic representation of a symmetrical Bouligand layup consisting of two Bouligand units with a pitch angle θ of 10°.

vancement and industrialisation of the spread-tow process as presented by Kawabe [8] and Sihn [9].

Very promising results for out-of-plane loads have been realised in previous studies. Mencattelli et al. [10] observed in their parameter study on different layer pitch angles for linear Bouligand structures a continuous improvement of the compression after impact strength with decreasing pitch angle. Reducing the pitch angle from 45° to 2.5° leads to a reduction of 29.4° in projected damage area while retaining a similar CAI strength, with a considerably reduced number of 0° plies. The main damage mechanism in Bouligand laminates are twisting matrix cracks. Small pitch angles significantly reduce the formation of critical failure mechanisms such as delaminations due to reduced inter-laminar shear stresses. At the same time, crack growth in thickness direction is no longer limited by the surrounding layers. Matrix cracks propagate in the thickness direction, since the low inter-laminar shear stress prevents crack deflection into the inter-laminar boundary layer. By crack deflection and continuous change of the fracture plane in thickness direction, the crack path is extended and the energy dissipation during crack growth is increased [10–12]. The result is diffused, sub-critical helicoidal matrix damage. This sub-critical impact damage leads [7,11] to an increase in compressive residual strength compared to 45° pitch angle laminates of up to 8%[13].

Additionally to out of plane loading and residual strength, the in-plane tensile performance of CFRP-Bouligand structures is investigated in this study. In classical 45° pitch angle laminates with sufficiently thick plies delamination is the predominant failure mechanism. Delamination initiates at matrix cracks or at free edges and propagates through the inter-ply interface. Delamination steps through adjacent interfaces via transverse and off-axis matrix cracks, reaching the interface with the 0° plies, isolating them and thus leading to complete gauge section delamination of the interfaces adjacent to the 0° plies, resulting in early delamination failure [14–16]. In thin-ply laminates, the dominant failure mode changes to fibre failure [9,17]. As a result, the static tensile strength of notched thin-ply composites is decreased, because the lack of stress relaxation through damage leads to a higher stress concentration and premature failure compared to thick-ply laminates. In order to increase the notched strength and the failure properties of laminates, different studies investigated new layup designs with smaller angles than 45° and displayed their potential. Wu et al. [18] demonstrated pseudo-ductile tensile stress-strain behaviour in unnotched thin-ply $[\pm 25_2/0]s$ laminates, where the 0° plies are high-modulus fibres while the 25° layers are made up of intermediate modulus fibres. Central 0° ply fragmentation and dispersed delaminations have been identified as the main damage mechanisms. These damage mechanisms can also relive the stress concentration in notched laminates, resulting in an enhanced notched strength and reduced notch-sensitivity. Bouligand laminates can potentially offer a similar damage mechanism. When the fracture strain of the 0° layer is reached and the load is dispersed onto the neighbouring plies. Due to the low angle fibre angle deviation and thin 0° layer the neighbouring plies are able to take this load. However, as the ply strength is decreasing with increasing angle a significantly lower fracture strain can be expected with a quasi-isotropic (QI) Bouligand layup. Due to the low angle delaminations are unlikely and thus only matrix fracture and fibre failure are the only offered failure mechanisms. This and the additional load path due to multiple fibre angles makes the approach interesting for notched laminates. Apichattrabrut et al. [19] performed tensile tests on unnotched thick-ply on symmetrical helicoidal laminates with a pitch angle of 10°, resulting in laminates with a thickness of 6.35 mm. Twisting cracks begin in steps with the pitch angle to grow near the edges in the 90° layer. Starting from the edges, the twisting cracks are propagating in a double helicoidal formed fracture plane through the thickness of the laminate, while no delamination occurs. Fibre failure is widely dispersed. Additionally the bending properties of thin-ply helicoidal laminates is evaluated. Due to their low pitch angle, they display a anisotropy in bending stiffness and strength. Cheng et. al [20] investigated the bending performance of thick-Ply glass-fibre-epoxy Bouligand structures with a pitch angle of 16.4° and found a similar flexible strength, but strongly increased residual strength after first damage initiation.

In view of the literature presented and topics investigated, we have conducted an experimental study to further investigate and adapt thin-ply Bouligand structures' mechanical properties. The novel investigations concerning the LVI and CAI properties are as follows:

- Bouligand thin-ply laminates with a ply angle of 2.07° are realised, which is the closest realised angle so far to the angles occurring in natural Bouligand structures.
- Determining the influence of the matrix's fracture toughness on the damage development, in order to determine whether a higher toughness has a beneficial impact on the damage behaviour.
- It has been shown that the sub-critical matrix damage in Bouligand laminates does not decrease the residual stiffness.

To further increase the impact resistance of Bouligand laminates, the Bouligand laminate is combined with an additional fibre-metal hybrid (FML) laminate section in the outer region of the laminate. The helicoidal layer structure of Bouligand laminates displays a substantial orthotropic bending stiffness. As a result, the laminate is significantly more rigid to bending in one direction than the other. Thin stainless steel metal foils are placed in the outer laminate areas. Due to the orthotropic bending stiffness of the helicoidal laminate and the FML section's high stiffness, the FML regions are subjected to high loads during impaction. On the non-impacted side of the laminate, the FML can offer

Table 1
Overview of the configurations considered, layup, resulting pitch angle and specimen thickness.

Configuration	Lay-up	Pitch Angle θ	Number of CFRP Layers n	Nominal Thickness [mm]
UNT (Neat)	$[a_1/a_2/\dots/\bar{a}_i]_S$			
OHT (Neat/Nano)		2.586	127	3.683
Bending (Neat)	with $i = \frac{n+1}{2} = 64$			
CAI/Comp (Neat/Nano)	$[a_1/a_2/\dots/\bar{a}_i]_S$			
		2.069	175	5.075
	with $i = \frac{n+1}{2} = 88$			
CAI/Comp (H1)	$\begin{bmatrix} M^S/a_1/a_2/a_3/ \\ M^S/a_4/a_5/a_6/ \\ M^S/a_7\dots/\bar{a}_i \end{bmatrix}_S$	2.169	167	5.023
	with $i = \frac{n+1}{2} = 84$			
CAI/Comp (H2)		2.169	143	5.023
	with $i = \frac{n+1}{2} = 84$			
45° Bending (Neat) Comparison	$[45°/90°/-45°/0°]_{22s}$	45	176	5.14

additional energy-consuming damage modes like plastic yielding and cracking, thus further decreasing the occurring matrix damage in the helicoidal laminate. Besides the impact properties also the tensile and bending properties of Bouligand layups are investigated. For the first time in the literature:

- Bouligand laminates were tested with an angle of 2.59° and thus the first time with an angle < 10° under tensile load and under < 16.8° for bending loading.
- A detailed damage analysis of the progressive damage development was performed using radiography and digital image correlation.
- The notch sensitivity of Bouligand laminates was investigated, and it was shown how the occurrence of sub-critical matrix cracks leads to a reduction in notch sensitivity.

The results highlight the potential of Bouligand layups in increasing the damage tolerance of composites.

2. Materials and specimen preparation

The laminates were manufactured from North Thin Ply Technology (NTPT) thin-ply prepreg with Toray S700SC-12K-60E fibres and NTPT Thinpreg 402 matrix. The main material used has an areal weight of 30 g/m^2 which results in a cured layer thickness of approx. 29 μm (see Table 1). Fig. 1 displays an representative mid-plane symmetric Bouligand structure as used in the present study, with a pitch angle of $\theta = 10°$ consisting of two Bouligand units. An odd number of layers was used throughout the study to obtain a centre-symmetrical laminate with a constant layer thickness in the mid-plane. The pitch angle θ can be calculated by:

$$\theta = \frac{360}{n-1} \tag{1}$$

where n is the total number of plies. The angle a_i of a certain layer i is determined by Eq. (2) with the pitch angle θ and total number of plies n:

$$a_i = \begin{cases} \theta \cdot (i-1) & 0 \le i < \frac{n+1}{2} \\ 360 - \theta \cdot (i-1) & \frac{n+1}{2} < i \le n \end{cases} \tag{2}$$

The different layups used are summarised in Table 1. $\bar{a}_i$ denotes the layer in the symmetry plane which is therefore half the thickness in this representation. M^S denotes the stainless steel foil layer. $0°^{1}20_{\frac{g}{m^2}2}$ and $90°^{1}20_{\frac{g}{m^2}2}$ denotes layers made from prepreg with a 120 g/m^2 areal weight. The different layups are explained in detail in the following.

For the layup of the UNT/OHT Specimens, the 0° fibre direction is chosen as an initial fibre angle to have the maximum amount of 0° in the load direction. The resulting layup is displayed in Table 1. The specimen dimension are chosen according to ASTM D 5776 [21] (see Table 2) and is comparable in thicknesses to a previous study, see Körbelin et al. [22], where thin-ply with an 45°-QI layup was investigated. Additionally to the neat matrix a Graphene-modified resin was also investigated. For this NTPT 402 resin modified with 0.5 wt. % few-layer graphene (FLG) was used. The nanoparticles used are Avangraphene 2 (Avan2) from the manufacturer Avanzare Innovación Tecnológica S.L. The addition of the nanoparticles leads to an increase in Mode I interlaminar energy release rate of 23.48% from 111.19 J/m^2 to 149.64 J/m^2 and in mode II interlaminar toughness increases by 34.58% from 574.42 J/m^2 to 709.03 J/m^2, see Körbelin et al. [22]. Specimen with the unmodified matrix are referred to “Neat” and with FLG-modified resin to “Nano” in the following. Three-point bending specimen were manufactured using the same layup, see Tables 1 and 2. For the compression specimen and the impact/compression after impact specimen four different configurations were investigated. Neat, Nano and two different FML layups. Dimensions were chosen according to ASTM D 7136 [23], see Table 2. The thickness was also chosen comparable to thin-ply 45°-QI layup investigated by Körbelin et al. [22]. The FML are Hybrid laminates consisting of Neat prepreg and an austenitic steel alloy. Each FML utilises six 1.4310 (X10CrNi18-8) C1300 cold rolled stainless steel layers with an 0, 03mm nominal thickness from Knight Strip Metals Ltd.. For the ”Hybrid 1” (H1) configuration, the steel layers were placed in the laminate’s outer area and separated by three layers of CFRP (see Table 1). The layup consists of two complete Bouligand units interrupted by two isotropic metal layers per unit and outer metal face sheets. The hybrid configurations used fewer CFRP layers to achieve approximately the same thickness as the Neat/Nano specimens. As a result, the pitch angle increases slightly. The steel layers are placed at the highest loaded regions during impact due to local deformation in the contact area with the impactor and high in-plane loads resulting from bending. They potentially offer new energy-consuming damage modes consisting of yielding and fracture. No steel layers were placed in the middle of the laminate for a couple of reasons. In the middle of the laminate, the in-plane stresses resulting from bending are minimal and consequently, metal layers cannot achieve the desired yielding behaviour. Additionally, the shear stresses τ_{13}, τ_{23} are the highest in the middle of the laminate [10] and interlaminar failure between steel layers and adjacent CFRP plies can lead to undesired delamination [24], because the inter-laminar strength of the steel-CFRP interface is lower than CFRP-CFRP. Delaminations have a more significant negative impact closer to the laminate’s midplane than on the outside. Thus metal layers in the middle of the Bouligand layup would negate their delamination suppression behaviour. The second configuration, “Hybrid 2” (H2), follows the same design philosophy in the regard that the metal layers are placed at the outside. However, the sub-laminates between the metal layers in the H2 configuration are not helicoidal layups (see Table 1). The outer of the two sub-laminates is 0° consisting of two 120 g/m^2 layers and the second is consisting of two 90° 120 g/m^2 layers. In the middle of the structure are two incomplete Bouligand units. The relatively thick, unidirectional CFRP layers can easily form matrix damage, promote local delamination from the metal layer and consume energy.

Table 2
Specimen dimensions and the according standards [21,23,28–30].

	Tension	Open Hole Tension	Impact / CAI	Compression	Bending
Standard	ASTM D3039	ASTM D5776	ASTM D7136/ASTM D7137	ASTM D6641	DIN EN ISO 178
Length [mm]	250	300	150	150	150
Width [mm]	25	36	100	25	
Gauge Section [mm]	150	200	–	10	150
Miscellaneous	GFRP	Hole Diameter	–	GFRP	
	Tabs	6 mm	–	Tabs	
			Nano: 4/3	Neat: 3	
Number of specimen	Neat: 8	Nano: 6	Neat: 4/3	Nano: 3	Neat: 4
		Neat: 3	H1: 2/1	H1: 3	45°-QI: 4
			H2: 2/1	H2: 2/1	

2.1. Specimen preparation

Rectangular, near net shape prepreg plies were cut with the desired angle with an Aristo TL1625 CNC cutter. During lamination, flat molds with an alignment jig were used to ensure precise pitch angles. The laminate was debulked every fourth layer for five minutes. The steel layers were pretreated to ensure sufficient adhesion between steel and epoxy resin matrix. [25] and [24] investigated CFRP and 1.4310 steel hybrids and found good results with 3M AC-130-2 surface treatment. Before treatment sheet steel foil was sanded with P500 sandpaper and thus deoxidised. The Water-Break Test was used to check the even sanding pattern. The layers were cut with a blank cutter so that the longer edge is perpendicular to the rolling direction. Afterwards the surface was cleaned with acetone and treated with AC-130-2 with the bath application procedure according to the manufacturer's recommendation.

The laminates were autoclave cured according to the manufacturer's specification. Cutting specimen to near-net-shape specimen geometry was carried out on specimen plates of the tensile and compression specimens in a CNC precision saw from ATM with corundum saw blade. The specimen geometry corresponds to the respective ASTM standards (see Table 2). The GFRP tabs for the UNT specimens were 1mm thick and 1.6mm for the compression specimens and bonded in a hot press using UHU Endfest 300. All specimen edges were polished up to P1000. After polishing, the holes for the OHT specimens were milled with an Isel Euromod three-axis milling machine. Before testing the specimens were dried in a vacuum oven at 40° for 12h. The specimens were then stored in standard lab condition for 7 days prior testing.

2.2. Experimental methods

For all tests, except the compression test, the displacement and strains were recorded using digital image correlation (DIC) with an Aramis 4M system from GOM GmbH. For this a high contrast pattern was sprayed onto the sample. All tests were performed using a Zwick-Roell Z400 universal testing machine. For the tensile test mechanical wedge clamps were used. Acoustic emission (AE) analysis system was utilised to determine the damage onset and the accumulated damage energy. The recording of AE data was carried out by using a Micro-II multi-channel acquisition system by MISTRAS. Two wideband differential sensors were used.

To evaluate the occurring damage, radiographs were taken using contrast media with a faxitron x-ray 43885 of Rohde & Schwarz. The radiograph was digitised with a transmitted light scanner. The impact damage was introduced using an uninstrumented drop tower from CEAST, equipped with an anti-rebound device. The impactor nose had a semi-spherical tip with a diameter of 20 mm. The specimens were placed on an aluminium frame with a 75 mm wide and 150 mm long cutout with 3 mm radius corners, which is according to ASTM 7136 [23]. The parameters of the impact process, such as mass and velocity, were chosen to correspond to the characteristics of LVI-impacts, see Richardson et al. [26] and Sjoblom et al. [27]. The impactor weight was 4.43kg and the drop height 0.345 m, which results in an impact energy of 15J.

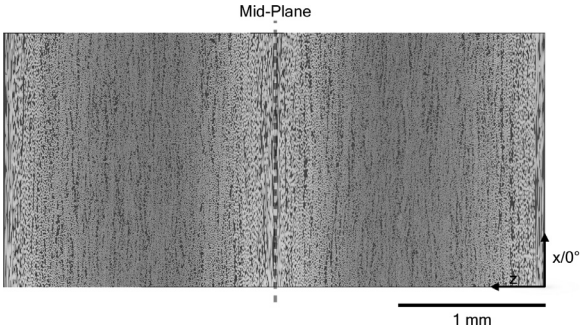

Fig. 2. Micro-section of a representative tensile specimen. The two Bouligand units symmetrical to the centre line are visible. The pitch angle of 2.857° enables a continuous fibre angle transition.

After impaction, several non-destructive and destructive test methods were applied to assess the damage in the samples and later evaluate the influence on the residual strength. Ultrasonic C-scans were carried out with a USPC 3040 DAC from Hillger NDT GmbH. The system has a resolution of 20 MHz and an amplification of up to 106 dB in 0.5 dB steps. Testing was performed with water as a coupling medium between the sample and an STS 6 MHz probe from Karl Deutsch GmbH. The ultrasound speed in the specimen was calibrated by measuring the sample thickness and adjusting the velocity until the measured thicknesses matched. With the back wall echo, the projected delamination area was determined. The image was converted into a binary picture using a threshold, which was kept constant for all scans. The area was then determined by inverting the binary picture and summing up the area of all black pixels. One specimen of each configuration was scanned using computed tomography after impaction, with a CT-Alpha device from Procon X-Ray GmbH, Germany. For the measurements of the neat and nano specimens an x-ray tube voltage of 140 kV without filtering was applied, while the measurements of the hybrid specimens were performed with a voltage of 200 kV and with a 1 mm Cu filter. All measurements were performed in axial mode with a voxel resolution of 60 μ m, resulting in a captured sample area of ca. 100 mm × 90 mm. Volume Graphics VGSTUDIO MAX 3.4 was used for the visualisation of the volume data.

The compression after impact strength was determined using a fixture according to ASTM D 7137 [28]. The compressive tests were performed using a combined loading hydraulic clamping, according to ASTM D6641 [29]. For the compressive specimen strain gauges from MICRO MEASUREMENTS of type CEA-06-250UWA-350 were used.

3. Results and discussion

3.1. Tensile specimen

Fig. 2 displays an representative microsection of a tensile specimen. Due to the low pitch angle of 2.59° no distinguishing of the different

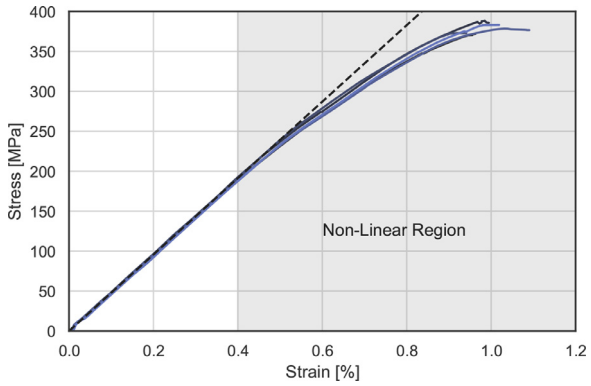

Fig. 3. Tensile stress-strain curves of the un-notched specimen. The grey area marks the non-linear response, which is defined by the AE-damage initiation.

Table 3
Tensile properties of the UNT-Tension specimen.

	σ_{Onset} [MPa]	$\overline{X}_t$ [MPa]	$\overline{E}_t$ [GPa]
UNT Neat	175.79 ± 12.39	382.76 ± 7.39	47.84 ± 0.72

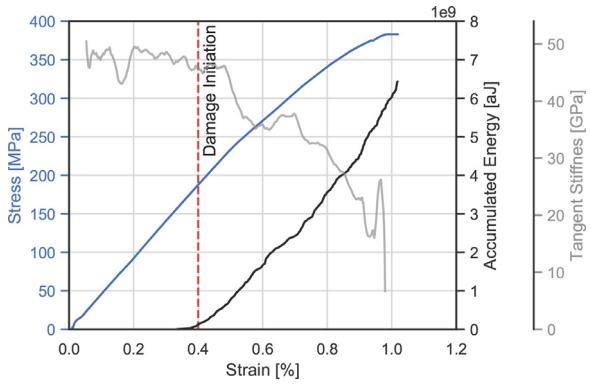

Fig. 4. Representative Stress-Strain curve of an un-notched specimen with the according accumulated energy from AE-measurements.

layers can be made. However, the laminate quality and consistency is visible.

Fig. 3 displays the structural response of the UNT specimens, the resulting mechanical properties are summarised in Table 3. The structural response is linear until a strain of 0.4%. Fig. 4 displays the stress strain curve of an representative tensile specimen in conjunction with the corresponding accumulated energy curve. The accumulated energy begins to increase significantly at a strain of 0.4% with a flat parabolic characteristic until fracture, which results in a damage onset stress of 175.79MPa. The damage onset stress in Table 3 is determined where the curve of accumulated energy begins to rise continuously.

The well known characteristic “knee” in the stress-strain behaviour of an FRP cross-ply laminate, can not be observed in the stress-strain behaviour. Hence, a seemingly continuous reduction in stiffness, which is caused by several inter-fibre cracks in the 90° layer, can be observed.

The X-ray images at different load levels, displayed in Fig. 5, show the crack development from the edges and continuous crack growth microscopically perpendicular to loading direction. The crack growth progresses in a micro zig-zag pattern, which indicates crack growth in different layers. The crack density increases with higher loads. However, in contrast to cross-ply or 45° pitch angle thick-ply laminates [31,32], the matrix cracks are not forming over the full width of the specimen. They form at the edge, grow into the laminate, but only up to a certain length. Cracks are initiated in the 90° layer and due to the occurring strain discontinuity damage is initiated at the same place in a different layer, but does not grow as the crack resistance of plies angled with smaller angles than 90° is to high. Only right before failure at 97.6%, white areas occur on the x-ray which could be mistaken for delaminations, however they mark opening helicoidal matrix cracks, which are also visible after failure (see Fig. 7).

Damage is increasing continuously, as the AE measurements show (see Fig. 4), the damage development does not occur suddenly, which is why there is a steady reduction in longitudinal stiffness and thus a flattening of the stress-strain curve. On closer inspection of the curve, it is noticeable that it is not decreasing with a consistent rate. Fig. 4 shows an typical stress-strain curve and a tangent modulus in the strain range of 0.07% to 0.93%. The tangent modulus is averaged over five data points and shows that the stiffness increases temporarily during the test. This stiffening effect can be accounted to fibre rotation. As matrix cracking occurs, fibres are able to slightly rotate into longitudinal direction and thus stiffening the structure. To enable fibre rotation, the matrix must yield or crack. The observed zig-zag pattern on the x-ray images shows shear cracking due to fibre rotation, indicating fibre rotation at the edge region of the specimens. The shear crack angle fluctuation shows the participation of many layers in crack propagation over the thickness. Calculation of updated fibre angle θ' as a result of fibre rotation can be done by Eq. 3 according to [33]:

$$\theta' = arctan\left(\frac{tan(\theta + \varepsilon_y)}{1 + \varepsilon_x}\right) \tag{3}$$

This equation states an rotation of the fibre angle in load direction for longitudinal positive strains ε_x and negative transverse strains ε_y. Fig. 6 shows that this is the case in regions at the edges of the specimen.

The non-linear stress-strain response results consequently on the one hand from matrix cracking, which reduces the tangent modulus and on the other hand from fibre rotation, which is increasing the tangent modulus. These two effects interfere and thus lead to a non-monotonically declining tangent modulus.

The fractured specimen of the an representative UNT Bouligand specimen is shown in 8. The shape of matrix failure is helicoidal and is following the layer rotation.

The fibre failure of the middle 0° and neighbouring plies is also exhibiting a helicoidal shape which is determined by the direction of fibre rotation. Fibre failure is initiated in the 0° layer and then propagates in the direction of the underlying fibre direction and thus turning with the pitch angle. The order of damage can be determined by the Xray and DIC pictures (see Fig. 5 and DIC 6), respectively. Matrix cracks begin to open, these cracks cause the bright shadow to appear on the X-ray images. This leads to excessive stress in the middle plies and finally to fibre breakage of the 0° ply in the middle. Subsequently, the laminate fails brittle in the outer sections. The brittle fracture is marked in red in Fig. 9. This failure sequence is also visible at the ε_x strain plot in Fig. 6. The plot after ultimate load shows a local strain increase in the fracture zone by mid section failure short before failure of the outer laminate sections occurs. The failure progression is not fully comparable to the pseudo-plastic failure observed by Fuller et al. [33] and Wu [18] as global strain to failure is significantly lower. This was to be expected due to the QI laminate design. However, some of the specimens exhibit a horizontal stress strain curve before failure (see Fig. 3), which indicates a similar effect to pseudo plasticity behaviour before failure. Fig. 9 shows a localised failure region. However, a cascading effect is visible. Due to the underlying fibre rotation, for one half of the specimen the fibre failure is not following the matrix cracks. But fibre failure is not purely brittle, as the fibre presumably fail first in the 0° layer, then in the 2.58° layer and so on until final failure is reached. This results in non localised failure, which is also reflected in the low standard deviation of the strength (see Table 3).

Fig. 10 qualitatively summarises the occurring damage modes and sequence during tensile loading of 45°-thick-ply, 45°-thin-ply and Bouligand thin-ply composites. The general behaviour can be described as

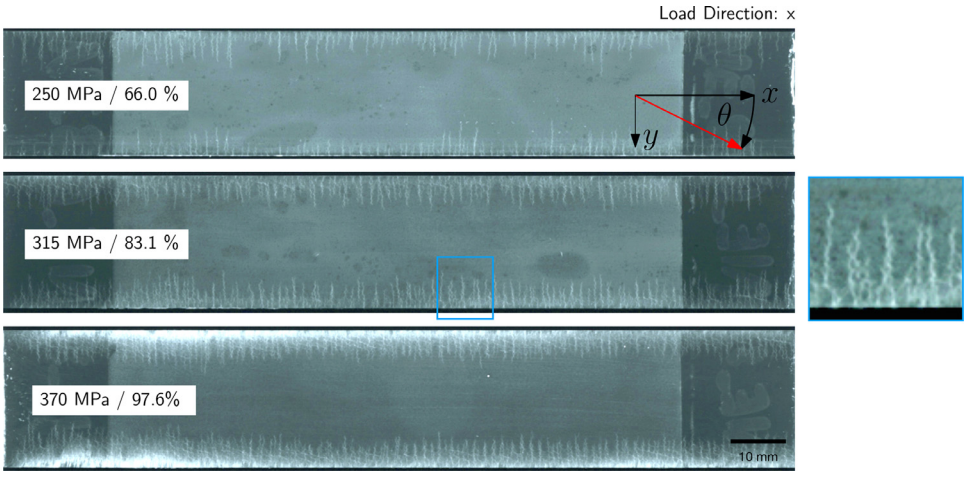

Fig. 5. Radiographs of an representative UNT specimen at increasing load levels.

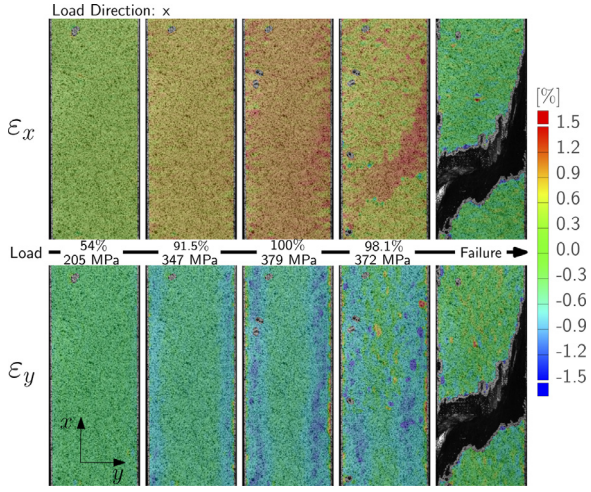

Fig. 6. Strain distribution at increasing load levels in tensile ϵ_x and transverse ϵ_y direction.

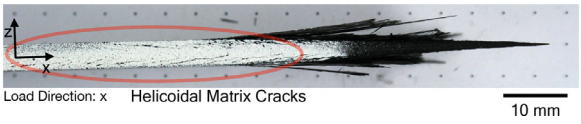

Fig. 7. Matrix cracks form in a rotating, helicoidal pattern at an even distance.

follows: For thick-ply composites, matrix cracking is the first occurring damage mode, however the damage characteristic is determined by delamination. 45° thin-ply laminates revealed that first-ply failure (FPF) is delayed nearly up to ultimate failure and thereby increasing the strength and design space considerably [9,17,34,35]. Additionally, delamination initiation at matrix cracks or at free edges is delayed or even suppressed [9,17,36,37]. The Bouligand layup suppresses all damage modes, except matrix cracking before fibre-failure. However, Table 3 reveals the low FPF strength of the Bouligand, which occurs between 44% and 47% of the ultimate load, whereas 45° thin-ply layups achieve a significantly higher FPF at ≥ 90% of the ultimate load.

3.2. Open-Hole Tension

Fig. 11 displays the stress-strain responses of the OHT specimens. Generally the characteristics are similar to the UNT specimens, compare Fig. 3.

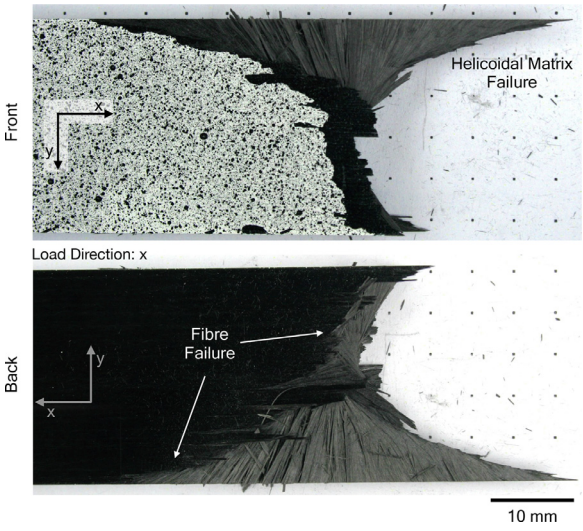

Fig. 8. Fracture area of an OHT specimen. Helicoidal shaped matrix failure and distributed fibre breakage is visible.

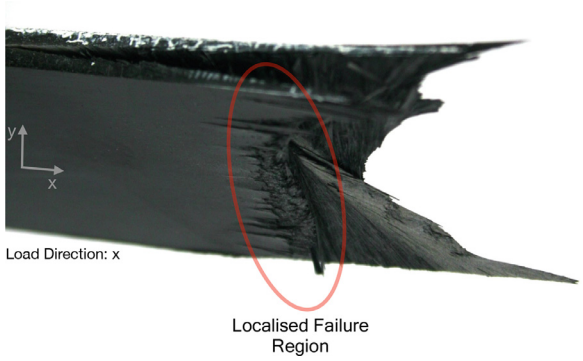

Fig. 9. Fracture of an UNT specimen. Fibre fracture distribution on the outer layers depends the direction of the fibre rotation of the layup. It is partially distributed while the rest is localised.

The properties resulting from the tensile tests are summarised in Table 4. Fig. 13 presents the damage development in a representative OHT neat specimen with increasing load. Similar to the UNT specimen, cracks grow from the specimen edge into the specimen (compare Fig. 5). The shape is also helicoidal (see Fig. 12), as the matrix cracks follow the fibre rotation.

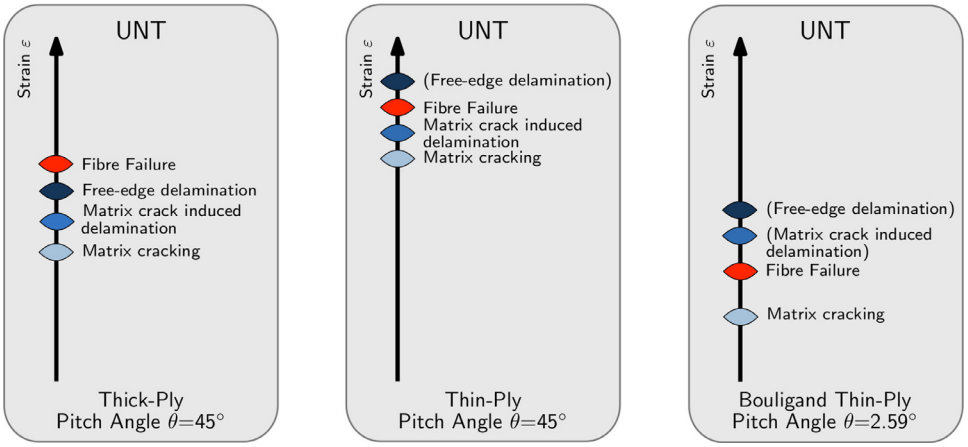

Fig. 10. Qualitatively visualised damage sequence of UNT 45°-QI thick-ply, 45°-QI thin-ply and Bouligand-thin-ply.

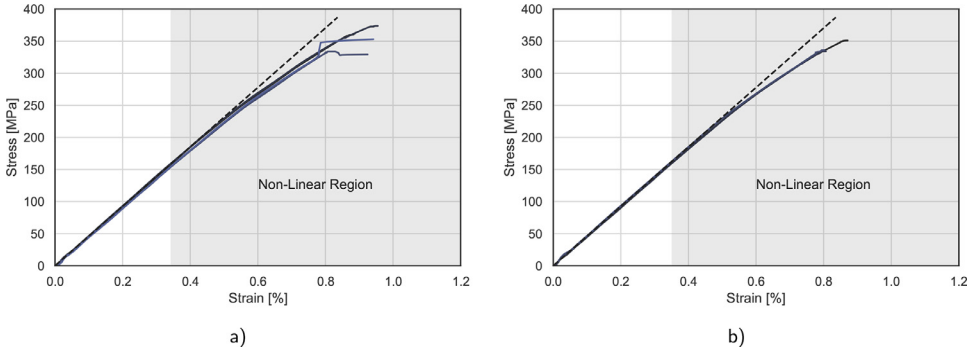

Fig. 11. Stress strain curves of the Neat OHT specimen (a) and Nano OHT specimen.

Table 4
Tensile properties of UNT- and OHT specimens.

	σ_{Onset} [MPa]	$\overline{X}_t$ [MPa]	$\overline{X}_{t,net}$ [MPa]	$\overline{E}_t$ [GPa]	k_F
OHT Neat	159.10 ± 16.10	360.02 ± 16.49	431.06 ± 19.76	46.37 ± 1.10	0.941
OHT Nano	163.01 ± 23.43	342.05 ± 9.41	414, 42 ± 11.38	46.13 ± 0.19	0.894
UNT Neat	175.79 ± 12.39	382.76 ± 7.39	-	47.84 ± 0.72	-

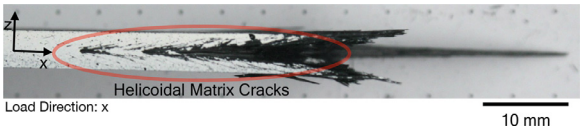

Fig. 12. Matrix cracks form in a rotating, helicoidal pattern.

Additionally cracks are initiated at the hole (see Fig. 13). Due to the high shear loads in low angle plies, shear matrix cracking occurs and initiates transverse cracks in other layers. This leads to a spread of damage over a larger area from the hole when the load is increased. However, compared to thick-ply 45° pitch angle laminates, the shear cracks in low angle layers are not able to easily propagate, as the crack growth resistance increases with crack propagation, as the helicoidal layup twists. This effect limits the damage propagation significantly. When viewed from the centre of the hole at increasing loads, the longitudinal shear

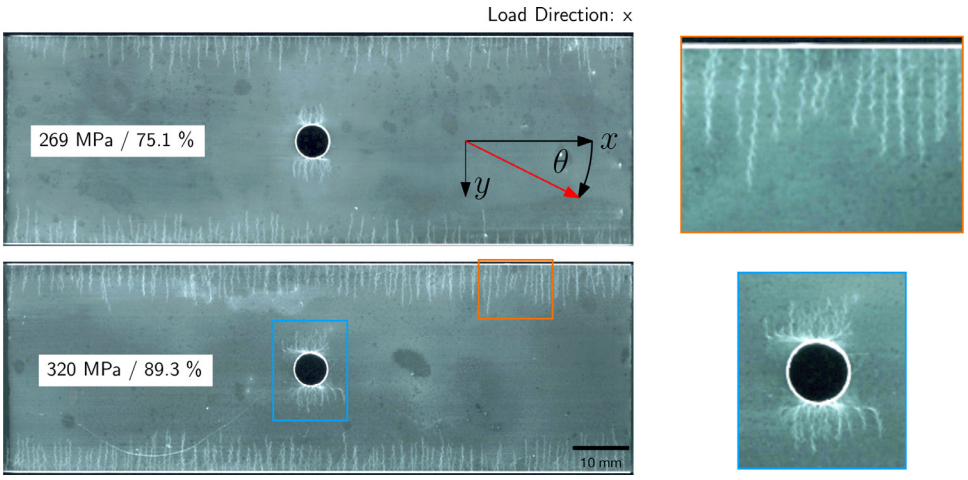

Fig. 13. Radiographs of an representative OHT specimen at increasing load levels.

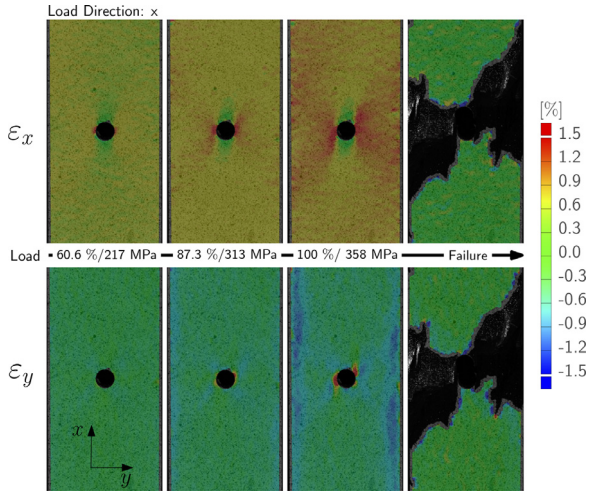

Fig. 14. Strain distribution in OHT specimens with increasing load in tensile ε_x and transverse ε_y direction.

Table 5
Accumulated acoustic energy at failure by AE Measurement.

Type	Total Accumulated Energy [pJ]
UNT Neat	6109.12 ± 264.66
OHT Neat	6729.67 ± 299.28
OHT Nano	4644.77 ± 236.12

Table 6
Comparison of the tensile properties of Bouligand and 45°-QI layups.

	σ_t^{onset} [MPa]	σ_t^{max} [MPa]	σ_{net}^{max} [MPa]	k_F
OHT Bouligand Neat	159.10 ± 16.10	360.02 ± 16.49	431.06 ± 19.76	0.941
OHT 45°-QI Neat 30 g/m^2	342.66 ± 5.05	391.10 ± 4.92	467.44 ± 5.98	0.42
OHT 45°-QI neat 120 g/m^2	298.54 ± 25.04	499.18 ± 15.578	431.06 ± 19.76	0.50

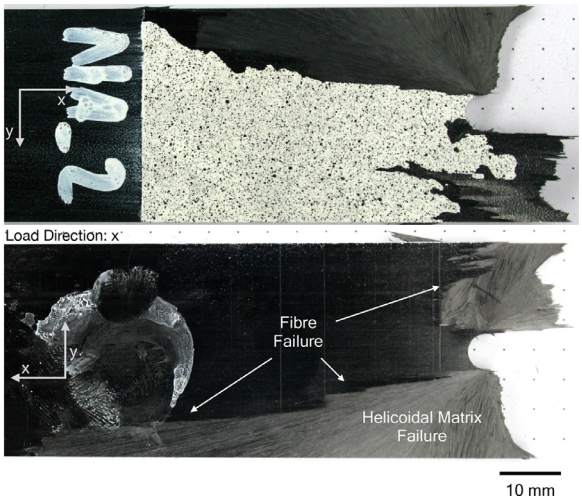

Fig. 15. Fracture area of an OHT specimen. Helicoidal shaped matrix failure and distributed fibre breakage is visible.

crack is developing in longitudinal direction, but only on the right hand side with a deflection of propagation direction in pitch angle direction. Since the longitudinal cracks are only visible on the right hand side, they are only initiated in the outer 0°- and adjacent layers.

This effect can also be observed in contour strain plots derived from the DIC (see Fig. 14). Damage initiates in the layers with angles close to 90°. With increasing load, shear induced matrix cracking spreads the occurring matrix damage over a large portion.

The load shadow resulting from the hole can be seen in Fig. 14 in front and behind the hole in load direction. The shadow rotates to the right as the load increases and follows the direction of layer rotation. Accordingly, the strain distribution is asymmetrical in the vicinity of the hole. At the edge regions, the strain distribution is similar to the unnotched case. Diffuse matrix cracking is also present at the hole, but also subjected to the through-thickness anisotropy of the laminate, see x-ray images in Fig. 13.

Table 4 reveals that the notch sensitivity k_F is low, as the ratio of OHT far field strength to UNT strength is almost one. The OHT strengths $\bar{X}_t$ are calculated in relation to the cross-sectional areas of the test specimens without taking the hole into account. The strength values related to the net-section area are the notched strengths $\bar{X}_{t,net}$. When comparing the x-ray images in Figs. 5 and 13, the crack density in net-sections next to the hole is significantly higher compared to the unnotched specimens. The higher crack density leads to the reduction of stress concentrations and thus delay the fracture. This assumption is supported by comparing the strength values of Neat and Nano specimens, as the Nano specimens display a lower OHT strength (see Table 4). Table 5 summarises the mean cumulative energy dissipation of the specimen configurations as determined by the AE-measurement during the test until failure. The dissipated energy of the Nano specimens is only 71.5% of the Neat specimens, which indicates lower damage until final failure. This behaviour can be accounted to the higher ERR of the Nano material. The higher ERR delays crack development and progression as a result fewer cracks are formed. Therefore, it can be derived, that the ERR is an important material property to consider when designing Bouligand structures. Consequently, appropriate ERR values need to be found in future research, which allow dispersed damage to form and thereby dissipate energy, while sustaining structural integrity. The optimal ERRs are thereby dependent on many influencing factors, like, e.g. fibre type, layer thickness, pitch angle and loading scenario.

The failure appearance of the OHT specimen is similar to the UNT specimen (see Figs. 12 and 16). The fibre fracture distribution depends on the direction of the fibre rotation of the layer structure. One half is strongly distributed while the other half is localised.

Table 6 compares the data of the OHT Bouligand layups to 45°-QI neat specimens with areal weights of $30 g/m^2$ and $120 g/m^2$ made from the same constitutes [22]. The data summarises the advantages and disadvantages of the Bouligand layup. Damage onset is considerably lower, as it is almost double for both 45°-QI layps with different layer thicknesses. Yet, the far field strength and the net-section strength are similar. This is remarkable, as the 0° fibre angle proportion is considerably lower. Also the low notch sensitivity factor is put into perspective, as the Bouligand neat specimens display a notch sensitivity factor of $k_F = 0.941$, the 45°-QI 120 g/m^2 of $k_F = 0.941$. The notch sensitivity of the Bouligand layup is also significantly lower than the notch sensitivity $k_F = 0.76$ reached by Wu et al. [18] with the pseudo-plasticity approach, which highlights the potential of small angles.

The failure behaviour of the different layups is also qualitatively summarised in Fig. 17.

3.3. Bending

Fig. 18 displays the bending stress-strain curves of the Bouligand and 45°–30 g/m^2 pitch angle laminates.

The derived mechanical results are summarised in Table 7. Due to the higher anisotropy of the Bouligand laminate in bending than the 45° pitch angle, the bending stiffness in the tested laminate direction is significantly increased. The bending strength however, is lower.

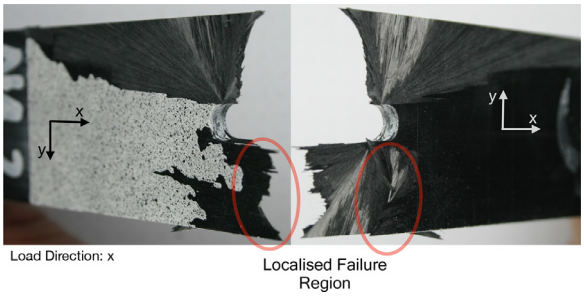

Fig. 16. Fibre fracture distribution depends on the direction of the fibre rotation of the layer structure. One half is strongly distributed while the other half is localised.

Table 7
Bending properties of Bouligand compared to a 45°-QI layup.

	$\overline{Y}_f$ [MPa]	$\overline{\varepsilon}_{f,max}$ [%]	$\overline{E}_f$ [GPa]
Classic-QI	907.77 ± 30.52MPa	2.48 ± 0.11%	41.772 ± 5.12GPa
Bouligand-QI	586.54 ± 16.84MPa	1.86 ± 0.02%	46.201 ± 2.83GPa
	−37.4%	−25.0%	+10.6%

Fig. 19 displays failed bending specimens of the two configurations.

Matrix failure is initiated in or close to the 90° layer of the lower Bouligand unit and consequently steps trough the outer tensional loaded layers, subsequently reducing the bending stiffness (see Fig. 18). The load drops suddenly, when the 0° fibres and fibres with angles close to 0° fail. Due the underlaying helicoidal matrix damage, the tensile-fibre failure is non-localised, similar to the tensile specimen (see Fig. 15). The strength of the Bouligand laminates is 37.4% lower than the 45°-QI layups. However, after failure the load carrying capabilities are fully lost, as the laminate has fully separated. The 45°-QI layup displays different failure modes (see Fig. 19). They either split and fail catastrophically or fail in a combination of compressive failure and delamination. The fracture behaviour of the Bouligand lay up is good-natured and does not show catastrophic failure. From a fail-safe point of view, the Bouligand structure is considered more favourable. There is no danger of layer delamination and a limited residual loading capability is retained. Besides with a high probability of impact damage such behaviour is suited for crash elements.

3.4. Low-velocity impact

The damage resulting from LVI for the Bouligand structures is characterised by the formation of matrix damage. With the chosen impact parameters no fibre failure is visible. The projected damage area, obtained by the C-Scans is summarised in Table 8. Here a strong reduction damage area compared to 30 g/m^2 45°-QI laminates is found. For all tested configurations the projected damage is reduced at least to 55.40%.

Table 8
Projected Damage Area of impacted CAI specimens.

Type	Damage Area [mm^2]	Normalised to 45°-QI [%]
45°-QI Neat 30 g/m^2	5881, 35 ± 1323.66	100
Bouligand Neat	2746.56 ± 350.25	46.70
Bouligand Nano	3258.17 ± 293.64	55.40
Bouligand Hybrid 1	3144.43 ± 193.71	53.46
Bouligand Hybrid 2	2836.37 ± 371.89	48.23

As opposed to C-Scans and radiographs the CT measurements enable to 3-dimensionally image the damage pattern and thus distinguish damage features in different depths of the specimens. Fig. 20 shows a CT-scan of the occurring failure in neat specimen. Here the helicoidal shape of damage is visible. In the *y-z* plane the helicoidal twisting of the matrix cracks is visible. The cracks start in the top layer parallel to the x-axis and are then deflected with the twisting layer until the crack is stopped at a fibre angle close to 90° angle damage. However, in the x-z plane at a distance of 0mm, the same behaviour is visible only starting in the 90° layer. Whe n the crack gets deflected due to the twisting layers the angle between the x-axis and the crack is converging 0°, but not reaching it, thus not forming a delamination. The Nano specimen shows a slightly different failure behaviour. The increase in ERR leads to a reduction in overall damage, the crack density is significantly reduced, which is especially visible when comparing the cut through the impact point in the x-z plane. The Neat specimen hast a very high crack density especially in the lower half of the sample while the Nano specimen only shows a reduced number of cracks.

The steel layers complicate the CT imaging of the hybrid specimens due to the high x-ray absorption of steel. This results in increased image noise and artefacts adjacent to the steel layers, which reduce the capability to precisely segment and visualise the damage. On the other hand, C-Scans and radiography are compromised even stronger by the metal and cannot detect the damage pattern between the steel layers. However, the CT measurements can reveal the general location, shape, and size of the hybrid specimens' damages, which show a different failure behaviour compared to the neat/nano specimens. Additional failure modes occur, due to hybridisation. Fig. 22 displays the failure in the H1 specimen. In both cutting planes a crack through all three metal layer on the non-impacted side is visible.

The crack is visible in both cutting views is due to the fact that the cracks are not running parallel to the *x*-axis. Fig. 23 displays the

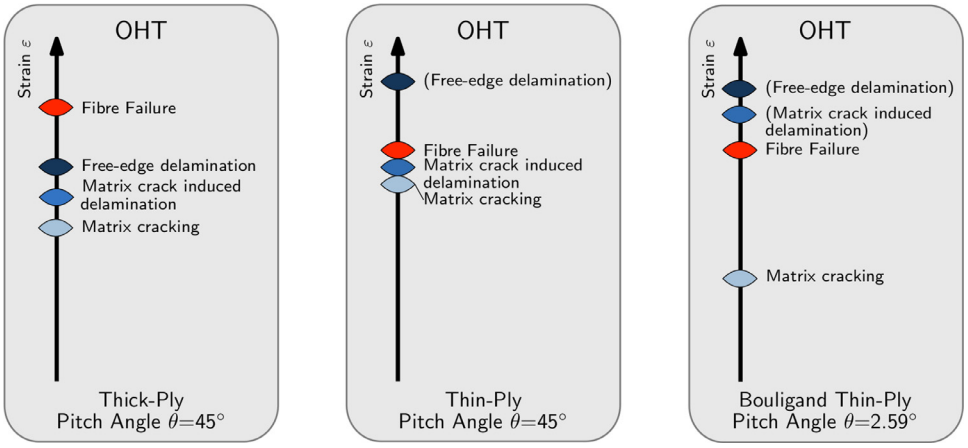

Fig. 17. Qualitatively displayed damage Sequence of OHT QI thick-ply, OI-thin-ply and Bouligand-thin-ply.

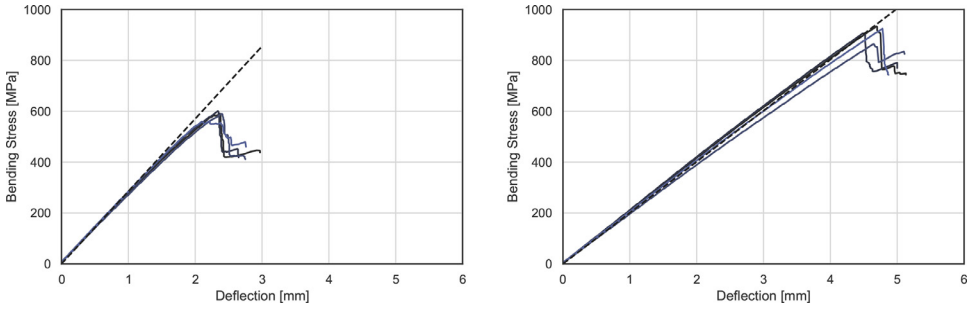

Fig. 18. Three-point bending stress-strain curves of thin-ply Bouligand and 45° pitch angle results.

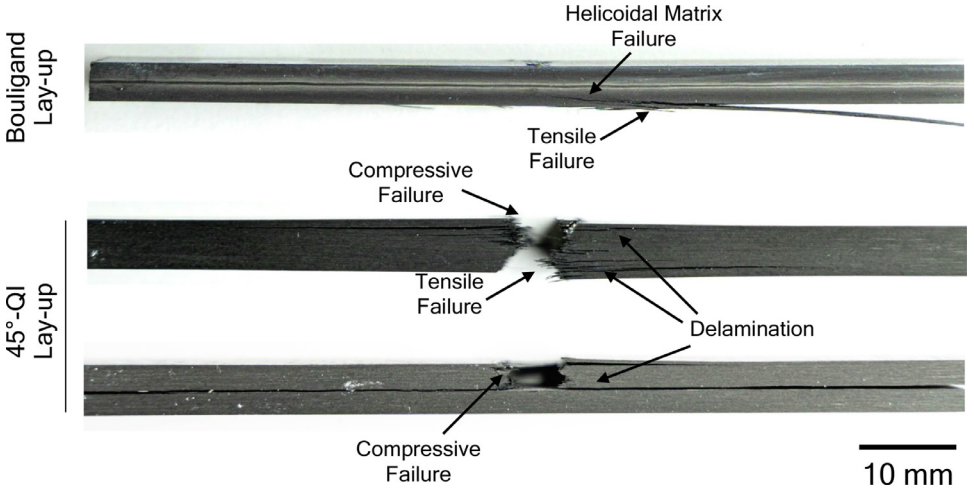

Fig. 19. Three-point bending failure of Bouligand and 45°-QI 30 g/m^2 layup.

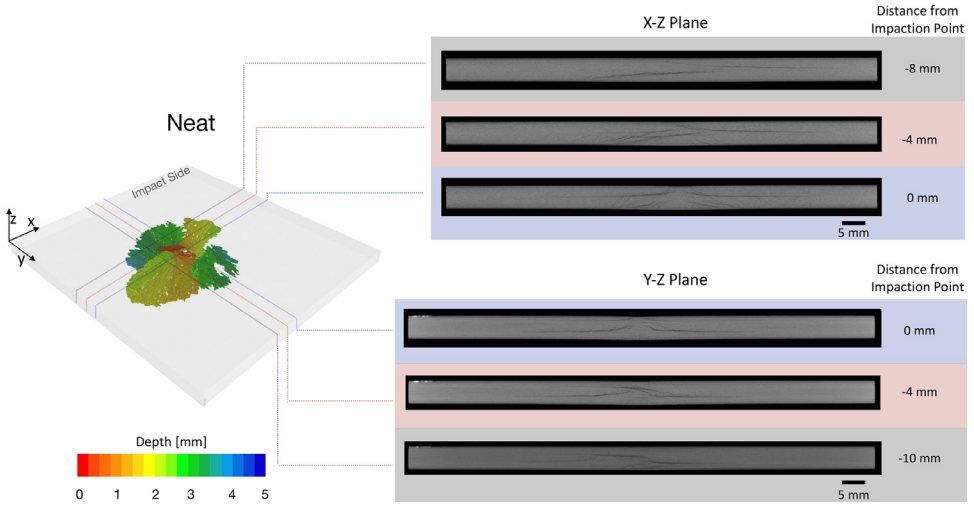

Fig. 20. CT image of the LVI damage in a Neat specimen. Displayed on the left is an overview image, and on the right are various cross-sectional presentations.

crack in the CAI specimen. The crack is twisting around the impact area. This confirms that the strength of the metal layers is fully utilised. In the CT-picture delamination of the metal foils from the laminate is visible along the crack, see *y-z* plane pictures. Additionally a delamination is also visible in the *x-z* plane at −4mm. This delamination is formed at the end of a helicoidal matrix crack. Overall the matrix damage is less severe, however delaminations form at the CFRP-metal interface, which are responsible for the larger projected damage area (see Table 8).

Fig. 24 displays the damage resulting from impact in the H2 specimen. Here the metal layer also exhibit a crack on the non-impacted side of the specimen. However due to the cross-ply layup the crack is following the fibre direction of the outer CFRP-layers. The 3D-CT-Image also reveals a accumulation of damage in the lower Bouligand unit below the 0° layer, which is a result of the higher bending stiffness resulting of the cross-ply layup in the cover laminates, as this is increasing the resulting shear stresses.

Fig. 25 compares the damage of the Neat, H1 and H2 configurations. Particularly in the H1 configuration, a reduction in matrix damage is visible compared to the Neat configuration. As described above, in nature the Bouligand structure is combined with an additional impact, herringbone shaped region. Mencattelli et al. [38] replicated this with thin-ply composites and realised a further reduction in projected damage area of 71%. However, with the hybrid layup the reduction in matrix damage is difficult to quantify, as the projected damage area determined with the ultrasonic C-Scan is influenced by delaminations.

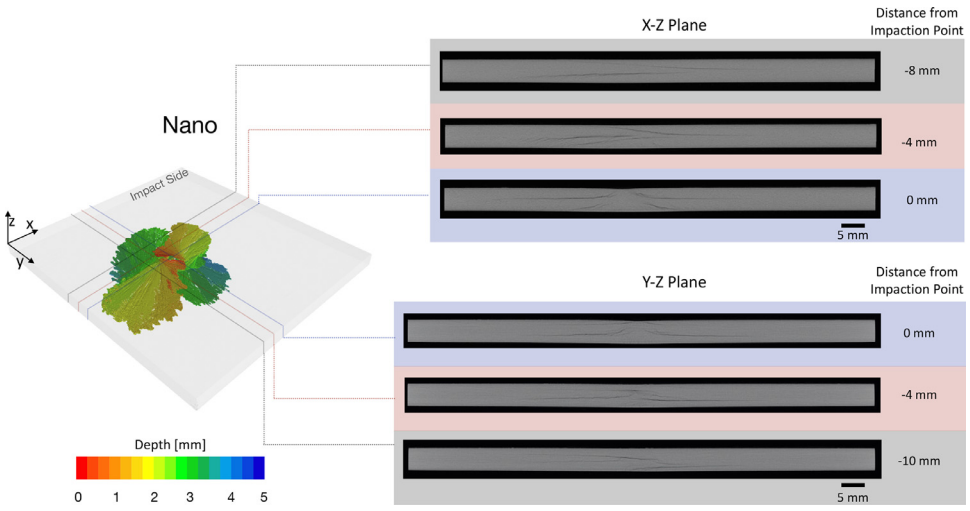

Fig. 21. CT image of the LVI damage in a Nano specimen. Displayed on the left is an overview image, and on the right are various cross-sectional presentations.

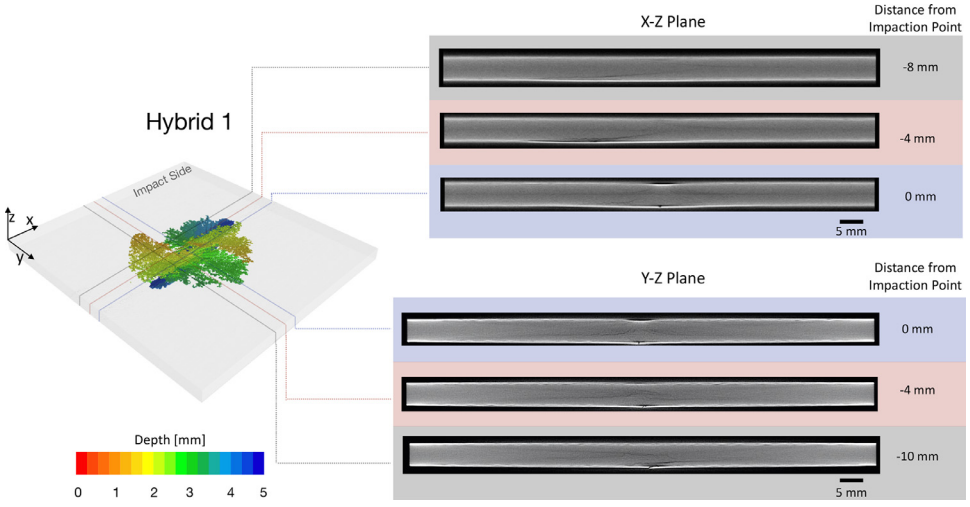

Fig. 22. CT image of the LVI damage in a H1 specimen. Displayed on the left is an overview image and on the right are various cross-sectional presentations.

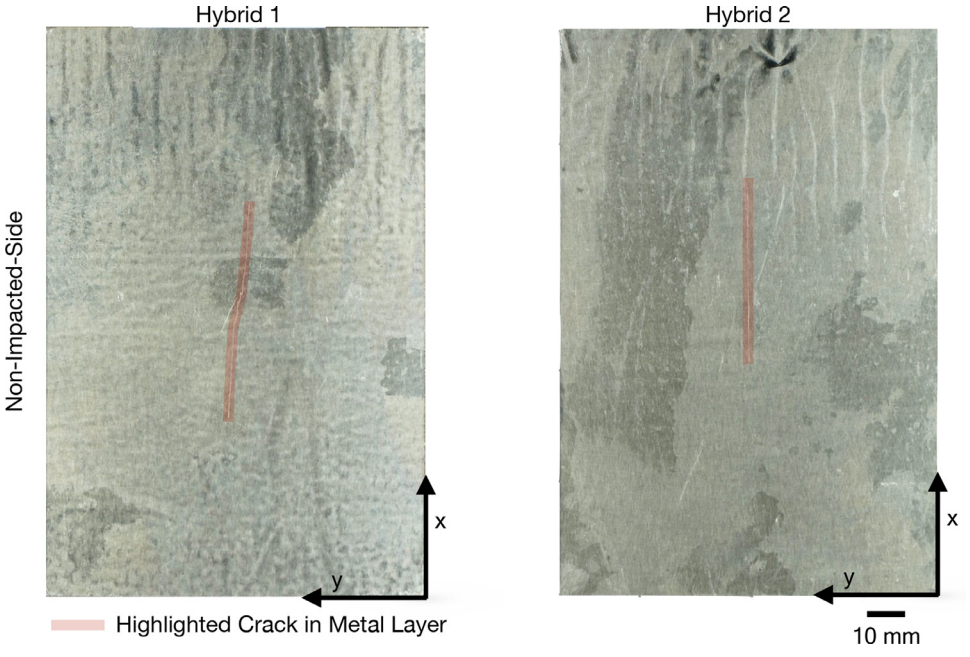

Fig. 23. Photograph of the surface of the non-impacted side of the specimen.

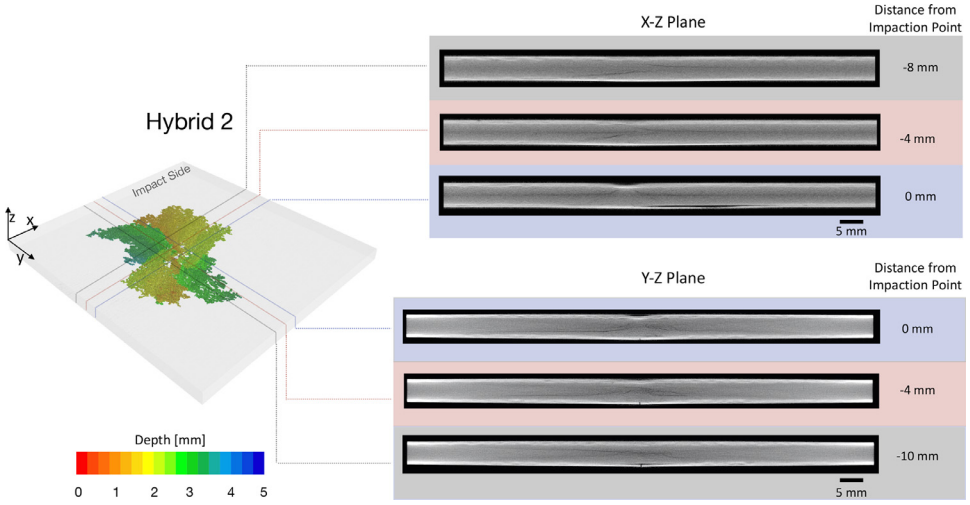

Fig. 24. Tomography image of the LVI damage in a H2 specimen. Displayed on the left is an overview image and on the right are various cross-sectional presentations.

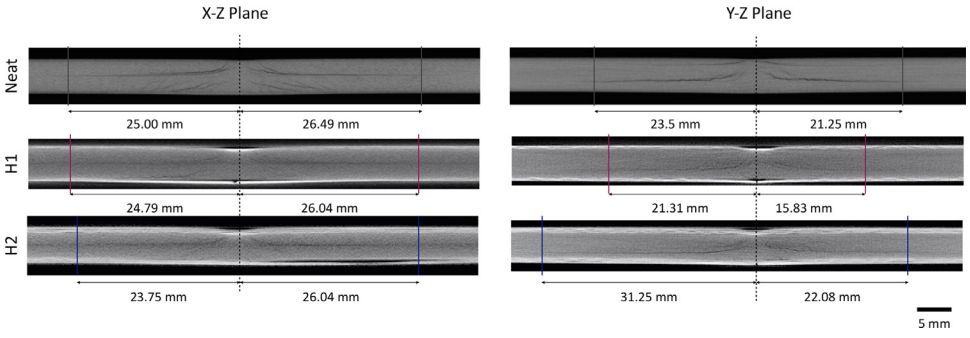

Fig. 25. Comparison of CT-Images from the section through the impaction point.

Table 9
Properties of Bouligand compression and CAI specimens.

	$\overline{X}_c$ [MPa]	$\frac{\overline{X}_c}{\rho}$ [10^{-3}MPam^{3}kg^{-1}]	$\overline{E}_c$ [GPa]	Strength Retention [%]
Comp. Neat	492.33 ± 2.53	274.89 ± 1.62	42.67 ± 2.5	
Comp. Nano	428.56 ± 25.08	274.34 ± 16.06	46.47 ± 1.96	
Comp. Hybrid 1	455.25 ± 23.75	255.57 ± 13.33	49.69 ± 0.85	
Comp. Hybrid 2	450.23 ± 34.58	249.99 ± 19.20	43.56 ± 1.92	
CAI Neat	194.63 ± 7.49	124.62 ± 4.79	44.62 ± 2.71	39.53
CAI Nano	193.81 ± 8.21	124.07 ± 5.28	46.97 ± 0.06	45.22
CAI Hybrid 1	194.37	109.21	50.06	42.70
CAI Hybrid 2	186.27	103.43	43.59	41.37

Table 10
Comparison of residual compressive strength against 45°-QI 120 g/m^2 thick-ply.

Type	CAI-Strength		Max. Z-Disp.	Modulus Retention
	$\overline{X}_c$ [MPa]	$\Delta\overline{X}_{c,ref}$ [%]	[mm]	[%]
Bouligand Neat	194.63 ± 7.49	14.8	0.729	≈ 100
Bouligand Nano	193.81 ± 8.21	14.3	0.749	≈ 100
Bouligand Hybrid 1	194.37	14.7	0.804	≈ 100
Bouligand Hybrid 2	186.27	9.9	1.625	≈ 100
45°-QI Neat 30 g/m^2	176.52 ± 1.7	4.2	4.47	58.30
45°-QI Nano 30 g/m^2	177.65 ± 9.17	4.8	5.105	61.31
45°-QI Neat 120 g/m^2	169.50 ± 6.64	–	1.08	57.89

3.5. Compression after impact

Table 9 summarises compression and residual compressive strength of the different configurations. The compressive strengths are higher than the tensile strength, which is caused by the early matrix damage initiation under tension. The residual compressive strength lies between 186.27MPa and 194.63MPa, which results in strength retention between 39.53% and 45.22%. Despite the reduced damage the Nano specimen is not showing an increased residual strength, which can be explained by the fact that although fewer cracks form due to the higher ERR, the main cracks that determine the failure still form. This becomes clear when comparing the CT-images, compare Figs. 20 and 21. The strength values also reveal, that hybridisation does not have a positive effect on the compressive or residual compressive strength, especially when taking the higher density into account. Both in compressive testing and compression after impact testing the high stiffness of the steel layer leads to early delamination, which is reducing the strength considerably.

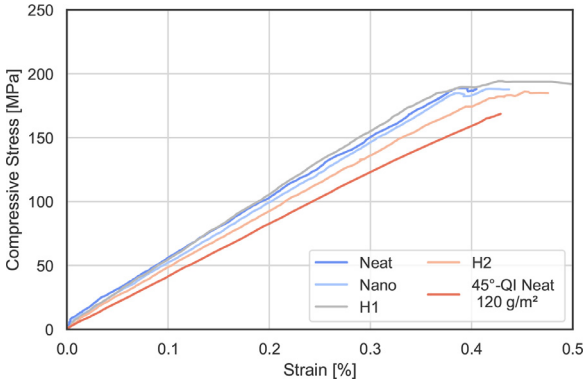

Fig. 26. Exemplary Stress-Strain curves of the tested Configurations and a 45°-QI Neat 120 g/m^2 specimen from [22] et al.

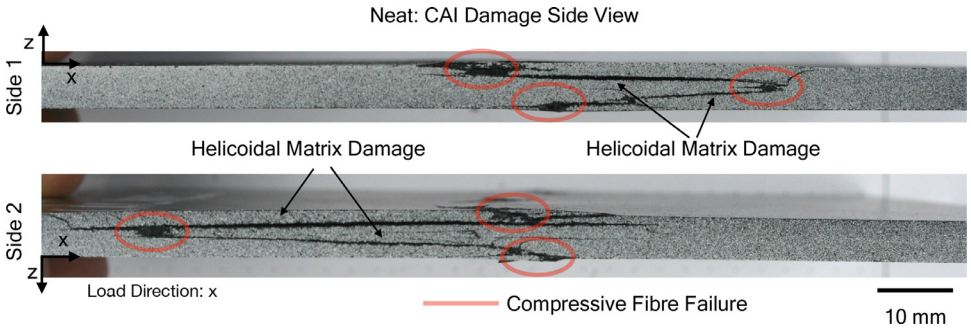

Fig. 27. Side view of the occurring damage modes of a Neat Bouligand specimen. Distributed, helicoidal matrix damage is visible. Fibre failure is following the matrix damage and is therefore distributed over a large area.

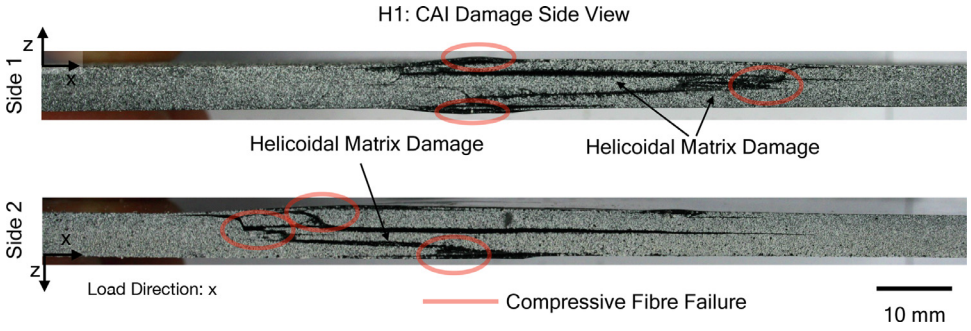

Fig. 28. Side view of the compression after impact damage of a H1 Bouligand specimen. Distributed, helicoidal matrix damage is visible. Fibre failure is following the matrix damage and is therefore distributed over a large area. Delaminations of the CFRP/Steel-sublaminates is visible where compressive fibre failure occurs.

Table 10 compares the obtained data of the Bouligand layups with data from 45°-QI layups. The residual compressive strength of Bouligand layups is up to 23% higher compared to the values obtained with 45°-QI layups, despite having less layers oriented in loading direction. This is, to the authors knowledge the best comparable performance of Bouligand structures in literature. The increase in residual strength can be accounted to the different governing damage modes. The failure of 45°-QI laminates is mainly determined by delamination failure and thereby stability driven failure. This is also visible in the residual modulus, as all Bouligand specimens show almost the same compressive modulus as the undamaged specimens (see Fig. 26 and Table 10). This is in contrast to 45°-QI laminate constructions, which only retain approx. 60% stiffness due to the delaminations causing local buckling. This damage characteristic results in a significant improvement in damage tolerance, as load redistribution initiates when the residual strength is reached and not as soon as the damage is present. This allows larger structures to remain fully functional up to a specific load level, even with impact damage.

The failure of the Neat and Nano specimen is very similar, therefore representative the failure of a Neat specimen is displayed in Fig. 27. The damage is characterised by helicoidal matrix damage and localised fibre failure. Failure is initiated at the helicoidal matrix damage, grows in loading direction and initiates final fibre failure. The failure is highly delocalised.

Fig. 28 shows the final failure of hybrid laminate H1. The failure is similar to the failure in the Neat and Nano specimen, compare Fig. 27. Non localised fibre-failure occurs combined with delaminations in the outer layer where the fibre-failure occurs.

Fig. 29 shows the failure of H2 specimen. The damage after final failure is not exhibiting non-localised matrix cracking and fibre failure. This can be accounted to the layup and the occurring failure modes of the H2 specimen, compare Table 1, Figs. 24 and 25. During residual compression testing the metal-layers delaminate at the impaction point due to their high stiffness and resulting high interlaminar stresses. When the load increases above the compressive strength of the laminate in between the hybrid top-layers final failure is initiated. Table 10 is showing the maximum Z-displacement of an representative CAI specimen before failure. Neat, Nano and H1 specimens exhibit a limited maximum Z-displacement, which can be accounted to the inner wedge resulting from helicoidal matrix damage pushing the outer layer into z-direction. H2 and especially the 45°-QI laminates exhibit higher z-displacements. In 45°-QI laminates the high z-displacement can be accounted to delamination driven stability failure. In H2, failure is a combination of severe top-layer delamination and local fracture in the region of the impact.

The presented results highlight that a conflict of objectives concerning the matrix damage properties for undamaged laminates, laminates with stress concentrations under tensile load and the residual strength after impact exists. The layup design that leads to the most beneficial matrix damage occurrence must be chosen according to the predominant, damage tolerance determining load case.

4. Conclusion

The damage tolerance results reveal the potential of the investigated thin-ply Bouligand layups. For example, Bouligand laminates with a pitch-angle of 2.07° have a 53.3% lower projected damage area than classic 45° quasi-isotropic laminates. No delaminations but only sub-critical matrix cracks occur. The suppression of delaminations leads to full stiffness retention in compression after impact testing. The residual compressive strength is 14.8% higher than 45° quasi-isotropic laminates, despite a lower proportion of 0° fibres in the load direction. Hybridisation with metal-layer leads to reduced matrix damage, but the residual strength is lower than non-hybrid CFRP layups, due to formation of local delaminations. However, the residual strength still exceeds the strength of 45° QI layups. The tensile properties are also noteworthy. The damage onset and tensile strength with 2.586° pitch angle are significantly lower than 45°-QI specimens. However, only limited sub-critical continuously increasing matrix damage develops before ultimate failure. Due to this sub-critical damage development, the tensile strength is barely affected by stress concentrations. The tensile strength is 2.5% lower for open-hole specimens than for the unnotched specimens, while the net-section strength increases. The OHT specimens achieve nearly the same strength as 45°-QI ply structures, despite a significantly lower 0° proportion of fibres. Bouligand bending specimen achieve a higher bending stiffness and predicable good-natured failure, but lower strength than 45°-QI specimens.

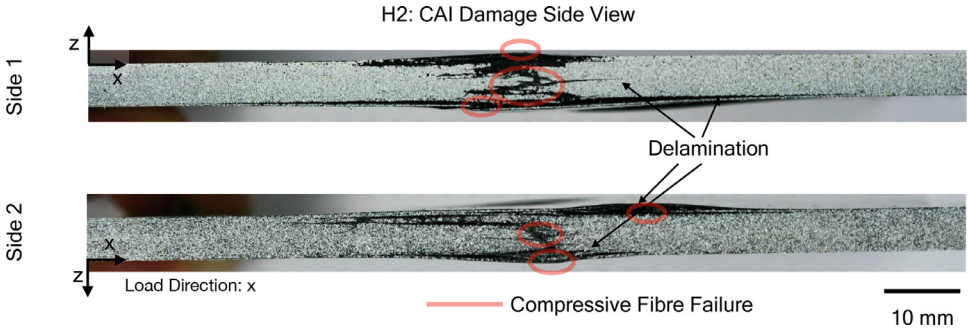

Fig. 29. Side view of the H2 Bouligand-Hybrid specimen after compression-after-impact testing. Compared to other configurations, localised failure and low degree of helicoidal matrix failure occurs. Distinct delaminations can be seen in the outer boundaries.

Declaration of Competing Interest

The authors declare that they have no known competing financial interests or personal relationships that could have appeared to influence the work reported in this paper.

Acknowledgement

This work was carried out with funding from the German Research Foundation (DFG) within the project number 283641236. This financial support is gratefully acknowledged.

References

[1] EASA, General acceptable means of compliance for airworthiness of products, 2010, Parts and appliances (amc-20), amc 20-29: Annex ii - amc 20-29 to ed decision 2010/003/r.
[2] Y. Aoki, H. I. Suemasu, T. Ishikawa, Damage propagation in CFRP laminates subjected to low velocity impact and static indentation, 2007, 16, 1, 45–61.
[3] J. Chang, V. Goyal, J. Klug, Composite structures damage tolerance analysis methodologies, 2012, Technical Report nasa/cr-2012-217347.
[4] Y. Bouligand, Twisted fibrous arrangements in biological materials and cholesteric mesophases, 1972, 4, 2, 189–217.
[5] G. Milliron, Lightweight impact-resistant composite materials: lessons from mantis shrimp, 2012, Dissertation|, University of California, Riverside.https://escholarship.org/uc/item/5zc2x10s.
[6] J.C. Weaver, G.W. Milliron, A. Miserez, K. Evans-Lutterodt, S. Herrera, I. Gallana, W.J. Mershon, B. Swanson, P. Zavattieri, E. DiMasi, D. Kisailus, The stomatopod dactyl club: a formidable damage-tolerant biological hammer, 2012. Science. 336, 6086,1275–1280,10.1126/science.1218764.
[7] L.K. Grunenfelder, N. Suksangpanya, C. Salinas, G. Milliron, N. Yaraghi, S. Herrera, K. Evans-Lutterodt, S.R. Nutt, P. Zavattieri, D. Kisailus, Bio-inspired impact-resistant composites, Acta biomaterialia 10 (9) (2014) 3997–4008, doi:10.1016/j.actbio.2014.03.022.
[8] K. Kawabe, T. Matszo, Z. Maekawa, New technology for opening various reinforcing fiber tows, 1998, 47, 7, 727–734.
[9] S. Sihn, R. Kim, K. Kawabe, S. Tsai, Experimental studies of thin-ply laminated composites, 2007, 67, 6, 996–1008.
[10] L. Mencattelli, S.T. Pinho, Realising bio-inspired impact damage-tolerant thin-ply CFRP Bouligand structures via promoting diffused sub-critical helicoidal damage, 2019, 182, 107684.
[11] H. Jiang, Y. Ren, Z. Liu, S. Zhang, Z. Lin, Low-velocity impact resistance behaviors of bio-inspired helicoidal composite laminates with non-linear rotation angle based layups, 2019, 214, 463–475.
[12] J.L. Liu, H.P. Lee, V.B.C. Tan, Failure mechanisms in bioinspired helicoidal laminates, 2018, 157, 99–106.
[13] F. Pinto, O. Iervolino, G. Scarselli, D. Ginzburg, M. Meo, M. Knez, Bioinspired twisted composites based on Bouligand structures, 2016, SPIE Proceedings of the Bioinspiration, Biomimetics, and Bioreplication 2016, SPIE. R.J. Martín-Palma, A. Lakhtakia, 97970E, 10.1117/12.2219088.
[14] M.R. Wisnom, S.R. Hallett, The role of delamination in strength, failure mechanism and hole size effect in open hole tensile tests on quasi-isotropic laminates, 2009, 40, 4, 335–342.
[15] B.G. Green, M.R. Wisnom, S.R. Hallett, An experimental investigation into the tensile strength scaling of notched composites, 2007, 38, 3, 867–878.
[16] S.R. Hallett, B.G. Green, W.G. Jiang, M.R. Wisnom, An experimental and numerical investigation into the damage mechanisms in notched composites, 2009, 40, 5, 613–624.
[17] R. Amacher, J. Cugnoni, J. Botsis, L. Sorensen, W. Smith, C. Dransfeld, Thin ply composites: experimental characterization and modeling of size-effects, 101, 2014, 121–132.
[18] X. Wu, J.D. Fuller, M.L. Longana, M.R. Wisnom, Reduced notch sensitivity in pseudo-ductile CFRP thin ply angle-ply laminates with central 0° plies, 2018, 111, 62–72.
[19] T. Apichattrabrut, K. Ravi-Chandar, Helicoidal composites, 2006, 13, 1, 61–76.
[20] L. Cheng, A. Thomas, J.L. Glancey, A.M. Karlsson, Mechanical behavior of bio-inspired laminated composites, 2011, 42, 2, 211–220.
[21] ASTM D5766 / D5766M-11, standard test method for open-hole tensile strength of polymer matrix composite laminates, 2018, 10.1520/D5766_D5766M-11.
[22] J. Körbelin, B. Kötter, H. Voormann, L. Brandenburg, S. Selz, B. Fiedler, Damage tolerance of few-layer graphene modified CFRP: from thin- to thick-ply laminates [accepted], Compos. Sci. Technol.
[23] ASTM D7136 / D7136M-20, test method for measuring the damage resistance of a fiber-reinforced polymer matrix composite to a drop-weight impact event, 2013, 10.1520/D7136_D7136M-15.
[24] D. Stefaniak, E. Kappel, B. Kolesnikov, C. Hühne, Improving the mechanical performance of unidirectional CFRP by metal-hybridization, in: Proceedings of the 15th European Conference on Composite Materials, ECCM15, 2012, pp. 1–8. Venice, Italy, 24-28 June 2012.
[25] B. Kötter, K. Yamada, J. Körbelin, K. Kawabe, M. Nishikawa, M. Hojo, B. Fiedler, Steel foil reinforcement for high performance bearing strength in thin–ply composites, 2021, 4, 100085.
[26] M. Richardson, M.J. Wisheart, Review of low-velocity impact properties of composite materials, 1996, 27, 12, 1123–1131.
[27] P.O. Sjoblom, J.T. Hartness, T.M. Cordel, On low-velocity impact testing of composite materials, 22, 1, 10.1177/002199838802200103.
[28] ASTM D7137 / D7137M-17, Standard test method for compressive residual strength properties of damaged polymer matrix composite plates. 2017, 10.1520/D7137_D7137M-17.
[29] 2016, ASTM D6641 / D6641M-16e1, Test method for compressive properties of polymer matrix composite materials using a combined loading compression (CLC) test fixture. 10.1520/D6641_D6641M-16E01.
[30] 2017, ASTM D3039 / D3039M-17, Test method for tensile properties of polymer matrix composite materials. 10.1520/D3039_D3039M-14.
[31] J. Berthelot, Transverse cracking and delamination in cross-ply glass-fiber and carbon-fiber reinforced plastic laminates: Static and fatigue loading, 2003, 56, 1, 111–147.
[32] J. Berthe, M. Ragonet, Passive infrared thermography measurement of transverse cracking evolution in cross-ply laminates, 2018, 54, 6, e12293.
[33] J.D. Fuller, M.R. Wisnom, Pseudo-ductility and damage suppression in thin ply CFRP angle-ply laminates, 2015, 69, 64–71.
[34] H. Saito, M. Morita, K. Kawabe, M. Kanesaki, H. Takeuchi, M. Tanaka, I. Kimpara, Effect of ply-thickness on impact damage morphology in CFRP laminates, 2011 30, 13, 1097–1106.
[35] A. Arteiro, G. Catalanotti, J. Xavier, P. Linde, P.P. Camanho, Effect of tow thickness on the structural response of aerospace-grade spread-tow fabrics, 2017, 179, 208–223.
[36] G. Guillamet, A. Turon, J. Costa, J. Renart, P. Linde, J.A. Mayugo, Damage occurrence at edges of non-crimp-fabric thin-ply laminates under off-axis uniaxial loading, 2014, 98, 44–50.
[37] M. Hajikazemi, W. van Paepegem, Variational analysis of free-edge stress and displacement fields in general un-symmetric and thin-ply laminates under in-plane, bending and thermal loading, Composites Part A, 2018, 113, 220–232. doi:10.1016/j.compositesa.2018.07.030.
[38] L. Mencattelli, S.T. Pinho, Herringbone-bouligand CFRP structures: a new tailorable damage-tolerant solution for damage containment and reduced delaminations, 2020, 190, 108047.